Automatic Hazard Detection for Landers

Andres Huertas, Yang Cheng and Larry H. Matthies
Jet Propulsion Laboratory, California Institute of Technology
Andres.Huertas@jpl.nasa.gov

Abstract

Unmanned planetary landers to date have landed "blind"; that is, without the benefit of onboard landing hazard detection and avoidance systems. This constrains landing site selection to very benign terrain, which in turn constrains the scientific agenda of missions. The state of the art Entry, Descent, and Landing (EDL) technology can land a spacecraft on Mars somewhere within a 20-100km landing ellipse. Landing ellipses are very likely to contain hazards such as craters, discontinuities, steep slopes, and large rocks, than can cause mission-fatal damage. We briefly review sensor options for landing hazard detection and identify a perception approach based on stereo vision and shadow analysis that addresses the broadest set of missions. Our approach fuses stereo vision and monocular shadow-based rock detection to maximize spacecraft safety. We summarize performance models for slope estimation and rock detection within this approach and validate those models experimentally. Instantiating our model of rock detection reliability for Mars predicts that this approach can reduce the probability of failed landing by at least a factor of 4 in any given terrain. We also describe a rock detector/ mapper applied to large high-resolution images from the Mars Reconnaissance Orbiter (MRO) for landing site characterization and selection for Mars missions.

1. Introduction

Landing site selection procedures in planetary exploration use all available remote sensing data to characterize the safety of potential sites before landing is attempted. With cameras now in orbit around Mars and planned to orbit Earth's Moon, it is possible to map all landing hazards larger than a few meters across. Planned precision navigation capabilities will allow avoiding such hazards based only on orbital mapping. However, slopes on the scale of a lander (e.g. < 6 m across) and rocks that could be fatal to a lander (eg. < 3 m in diameter and > 50 cm tall) may not be detected from orbit. Many sites of scientific interest on Mars, in the lunar highlands, and on other moons and asteroids have rock distributions high enough to create a landing failure probability of several percent for blind landers. In contrast, the Mars Science Laboratory (MSL) lander/rover in development for a 2009 launch will accept a landing failure probability due to rock impalement of only 0.25%. For a blind landing, this rules out well over half the surface of the planet. Recent imaging from the HiRISE camera on the Mars Reconnaissance Orbiter (MRO) for Phoenix mission landing site selection revealed high boulder concentrations near Mar's North Pole, areas previously considered benign for a lander. Therefore, increasing the accessible surface area requires even higher resolution orbital imagery and/or onboard landing hazard detection (HD) and avoidance capabilities.

Sensors options for HD have been studied for many years, including lidar, radar, and passive imaging [1,2]. Lidar and radar are attractive because they are direct ranging sensors applicable at relatively high altitudes. However, many factors make passive imaging attractive, including a shorter development cycle, potential for smaller size, lower power consumption and lower cost [2]. Landers typically carry descent cameras for scientific imaging that could also be used for HD. A navigation camera may also be needed at high altitude for landmark recognition for precision navigation. Such camera can also be used for HD.

There are still many passive imaging options, including use of color, texture, shading, structure from motion (SFM), stereo, and visible vs. thermal spectral bands. Any selected option also must have a statistical model of hazard detection performance that has been validated experimentally. The goal of modeling is to show that the probability of landing failure is within acceptable limits.

Section 2 examines planetary landing scenarios to identify a set of sensor/algorithm alternatives with

broadest applicability and to determine nominal sensor performance requirements. The conclusion is that stereo vision and shadow analysis appear to cover the widest set of missions with the least complexity. Section 3 summarizes algorithms we have developed to date for slope estimation and rock detection with these sensing modalities. Section 4 summarizes performance modeling and evaluation work for stereo-based and shadow-based hazard detection. Section 5 incorporates these results into an overall model of safe landing probability with these sensors. This work also represents a case study in vision system reliability modeling for autonomous navigation that is applicable to lidar and may be valuable in other contexts.

2. Landing Scenarios and Sensor Options

Mars is one of the most challenging places to do landing hazard detection because the rapid descent affords a short time for hazard detection and because the atmosphere constraints when sensing can be done and also reduces image contrast. Thus we use a Mars landing scenario as a design driver, since solutions that work from Mars should apply to most target bodies.

The descent sequence designed for the upcoming MSL mission provides a well-defined reference scenario. This includes a lateral divert maneuver starting about 1.2 km above ground level (AGL) and ending about 100 m AGL to get clear of the parachute; the lateral movement covers about 25% of the starting altitude. Doing precise terrain relative navigation (TRN) by map matching before this point will allow such a maneuver to be targeted to avoid large hazards known from orbital reconnaissance, such as craters up to ~ 100-200 m in diameter [3]. Detecting small scale hazards before or during this maneuver is impractical for several reasons: (1) it would be expensive because it would require very high sensor angular resolution over a wide field of regard, (2) it would require very accurate navigation to guarantee avoiding all small scale hazards from more than 1 km away, and (3) during the maneuver the high spacecraft attitude rates would make it difficult to obtain low smear, high SNR terrain images aimed at the right place(s) on the ground. At the end of this divert, descent is vertical and relatively slow, so HD is possible at this point to enable a second maneuver of 1-2 lander diameters to avoid small-scale hazards, such as rocks. Thus, performing HD at or below ~100 m AGL appears to be most practical for MSL-like missions.

With descent imagery, color, texture, and shape from shading are not promising for HD for a variety of reasons, including results from prior missions that show negligible color variation on asteroid Eros [5] and the impracticality of getting metric slope and rock size information with sufficient accuracy from texture and shading. Contrast in thermal imagery can discriminate rocks from soil over part of the diurnal cycle [6]. However, to minimize cost we would like HD and landmark matching to use the same camera; since the vast majority and the highest resolution orbital mapping imagery is visible spectrum, this is a disadvantage to using thermal imagery for HD.

Shadows can be used to recognize hazardous rocks from altitudes of 1 km or more [2], but this does not enable slope estimation. SFM can enable slope and rock detection if maneuvers are practical that give adequate parallax and enable aiming the camera at the landing site from two or more locations on the descent trajectory. This may be practical for missions to small bodies, like comets and asteroids, but it is costly and difficult for large bodies, like Mars. Binocular stereo baselines of ~1 m or more appear to be feasible for most landers and can enable slope and rock detection at altitudes up to about 100 m. Given that this fits the challenging reference mission scenario described above, stereo vision is our primary approach. Shadow analysis can augment rock detection for small incremental runtime cost and can significantly increase rock detection altitude for missions where that is needed, so we include shadows in our approach. Based on our current knowledge of hazard densities around the solar system, this approach is applicable to most or all lander missions. As we discuss below, the speed, reliability, and hardware maturity of this approach makes it a candidate for missions in about five years.

Interest remains in lidar for HD, particularly for robotic landers in permanently dark regions of the lunar poles and for crewed landers; however, it appears lidar is further from maturity for lander applications. The HD algorithms and performance modeling we apply to range data from stereo are applicable to lidar as well.

3. Hazard Detection Algorithms

We have developed three vision algorithms for the small scale hazard detection: (1) Stereo-based slope estimation; (2) shadow-based rock detection and (3) stereo-based rock detection. This section briefly summarizes the algorithms; the following section describes their performance.

Figure 1 shows a dataset used in many of our experiments. The stereo rig included two 1600x1200 cameras with a 1 m baseline and 22° x 18° FOV lenses.

At least 30 images were collected every 10m from 10m to 100m "altitude." Ground truth range data and Sun angles were also collected.

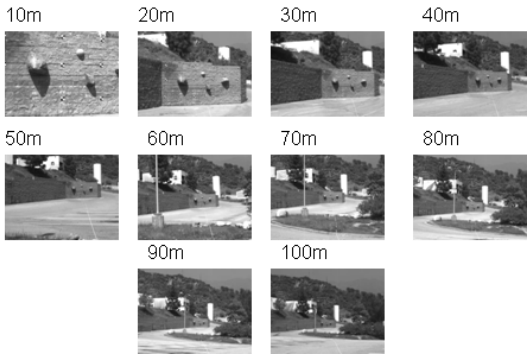

Figure 1. The wall dataset with ground truth used to evaluate stereo-based slope and rock detection and to supplement evaluation of shadow-based rock detection.

3.1 Stereo-based Slope Estimation

We use a real-time stereo algorithm that uses five overlapping correlation windows (SAD5) to produce high range data [7]. We have also implemented this algorithm in field programmable gate arrays (FPGAs) and expect to be able to make it operate on 1024x1024 pixel imagery at 10 frames/second (fps) or more. Figure 2 illustrates a stereo result applied to the wall data at 40 m altitude.

The slope estimation algorithm uses the stereo range data to produce a slope estimate by robust plane fitting. The algorithm has been tested with data that simulates "altitudes" up to 100m to produce slope error vs. latitude assessments relative to lander scale slopes. For plane fitting we first perform a least median square fit that includes the rocks on the surface, repeating the process for multiple triplets of points. If the median of the squared plane error is a minimum, we keep these points. Next we discard points far from the plane and apply a least squared fit to the remaining points to obtain the slope estimate. Figure 3 shows an example of plane fitting (red) applied to the wall range data (white) at 30m and at 70m.

3.2 Stereo-based Rock Detection

We first apply SAD5 stereo to obtain an elevation map and underlying surface plane. Then we apply rock detection in four steps (see Figure. 4):

1. Threshold the residuals from a robust plane fit.
2. The regions over the 1σ threshold are extracted. Then we estimate the deviation from the plane fit.
3. Extract potential rocks from connected components and discard noise regions.
4. Estimate rock height and position by averaging the 25 highest range points in each region to reduce noise in the estimates.

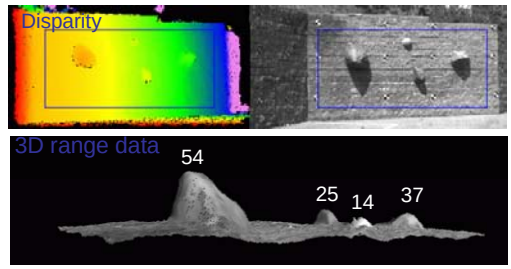

Figure 2. Sample SAD5 stereo vision range imaging results. Upper right: brick wall with synthetic rocks viewed from 40 m distance. Upper left: false color range image; red is closest and magenta is furthest. The overlaid rectangle shows the area used to evaluate plane fitting for slope estimation. Bottom: 3D rendering from below. The numbers above the rocks denote their true height in cm.

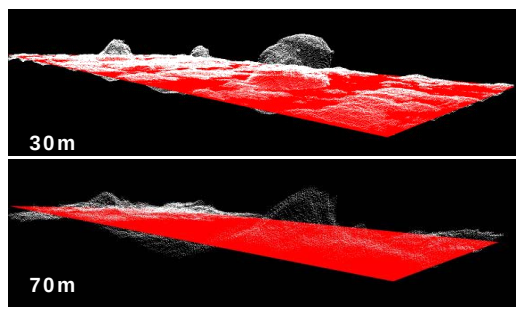

Figure 3. Surface plane fit applied to 3D stereo range data for two different altitudes.

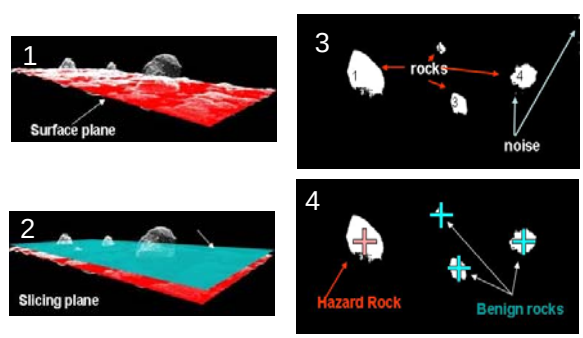

Figure 4. Stereo-based rock detection: 1) Robust plane fit to range data. 2) Threshold fit residuals at 1σ above surface plane. 3) Extract connected rock points. 4) Remove noise regions and estimate rock size and position.

3.3 Shadow-based Rock Detection

The ability to detect rock hazards at much higher altitudes than stereo can enable early detection of rocks in the scale of the lander and thus enables early assessment of hazards and diverts operations with reduced effects on the fuel budget. A possible target mega-pixel sensor (12° FOV) images a 1m diameter rock in 5 pixels at 1000 m, enables such early for rock hazard detection. The cues to the presence of rocks are the shadows they cast. Given a suitable range of illumination angles, shadow saliency and imager resolution this relatively straightforward vision task has become very useful to detect and map individual rocks.

The shadow-based rock detection algorithm has been described in detail in [2,3]. It consists of four steps, illustrated in Figure 5:

1. Image acquisition and parameters, e.g. Sun angles, shadow sensitivity and contrast estimate, ground sampling distance (GSD).
2. Shadow Segmentation. Shadows are segmented by applying a modified Maximum Entropy Thresholding (gMET) algorithm [2] that analyzes the histogram of a gamma-modified version of the input image to determine the threshold applied.
3. Shadow Analysis. The aim here is to represent shadow regions as a percept; we fit a "best-ellipse" [2] to the shadow regions that are larger than five 5 pixels. Shadows may be blended and merged. The real-time system does not attempt to segment the shadows individually but the rock mapper described later does.
4. Rock Modeling. A circular cross-section model (see Figure 5) is sufficient for our purposes. The parameters of the shadow ellipses combined with the Sun angle and GSD information to estimate shadow length and width, and rock model diameter, height and location.

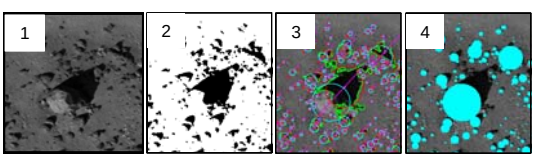

Figure 5. Sample results for shadow-based rock detection. 1) Input image. 2) Shadow regions. 3) Shadow analysis. 4) Rock

4. Hazard Detection Performance

4.1 Slope Error Analysis

The slope uncertainty model incorporates the following six factors (see Figure 6.) The stereo baseline (***dX***), the surface plane with respect to left camera, focal length (***f***), the correlation matching error, the size of measured surface patch, and the number of pixels on the surface plane. The mathematical details are given in [4a]. The 1σ slope error plots for the 10m to 100m span (see Figure 7) show that for the wall surface (5.6m by 2.8m) the slope error is smaller than 3° for 1σ at 100 m. The analytical model predicts that for a wall twice as large, the slope error would be smaller than 1.5^o at 100m.

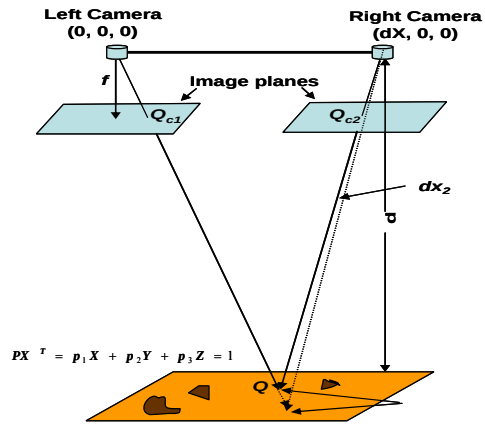

Figure 6. Stereo-based surface slope estimation model.

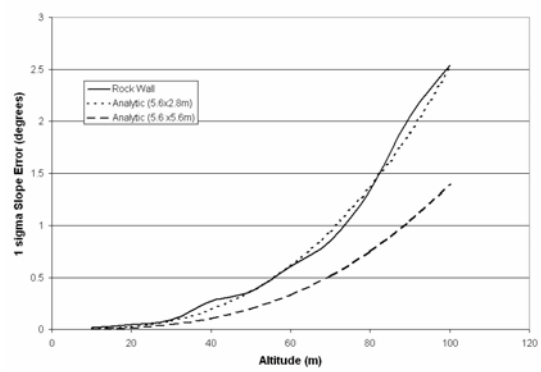

Figure 7. Surface slope estimation errors comparison between the analytical model and the experimental study.

4.2 Stereo-based Rock Detection

We have developed a model for rock detection and false alarm probabilities for the rock wall dataset specifically and compare the model to experimental results; in Section 5, we extend this to an overall model for the probability of a successful landing given a more general distribution of rock sizes at the landing site.

Our detection and false alarm models are based on Gaussian models of uncertainty in estimated rock heights above the nominal ground surface. To derive

these, we consider two more parameters for HD, illustrated in Figure 8. The first one denotes the lander rock tolerance *T*. A rock taller than *T* could cause a mission failure. The second one is the HD algorithm threshold *t*, used to decide whether a detected rock is a hazard. Given the uncertainty in rock height estimation, *t* is set below *T* to minimize missed detection of true hazards at the expense of an increased false alarm rate. An appropriate setting for *t* is then that which minimizes the probability of mission failure.

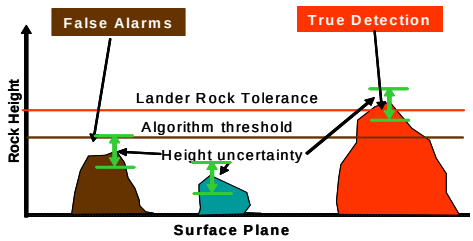

Figure 8. The lander rock tolerance threshold *T* and the HD algorithm threshold *t*.

The height uncertainty model treats rock height estimation as zero mean Gaussian with range uncertainty (σ). In theory:

$$\sigma = \frac{\boldsymbol{d}^2 \cdot \boldsymbol{ivFOV} \cdot \boldsymbol{k}}{\boldsymbol{dX}}$$

where ***d*** is the range in meters to the ground surface, ***ivFOV*** is the angular resolution of the sensor in mrad. ***k*** is the pixel precision, and ***dX*** is the stereo baseline in meters. The model uses a fixed number of range points on the ground surface as clutter, also represented by a zero mean Gaussian. The probability of detection, P_d, and the false alarm rate (***FAR***) are computed by integrating the tails of the Gaussian distributions. The experimental results using the wall data set and the analytical model are shown in Figure 9. Note that below 60 meters "altitude" stereo-based HD has almost perfect detection.

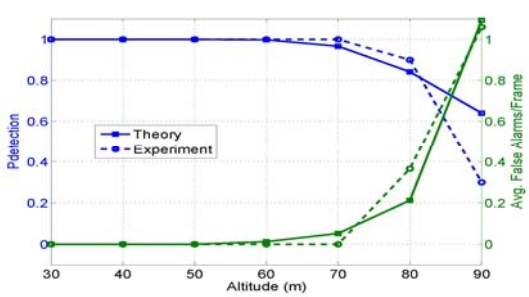

Figure 9. Hazard detection and false alarm rate comparison between analytical and experimental results from the wall dataset.

4.3 Shadow-based Rock Detection

We have tested shadow-based rock detection with aerial images of a rock field on Mars Hill in Death Valley, California. A small portion of one such image was shown earlier in Figure 3. The dataset does not have rock height ground truth, but it includes seven different sun incidence angles between 30° and 70° off nadir. We manually registered these images and constructed ground truth of 136 rock footprints by outlining rocks in one image. We averaged the detection and false alarm rates for the 136 reference rocks with diameters greater than 5 pixels over the seven sun incidence angles of the same location (shown in Figure 5.) The plots shown in Figure 10 summarize the results. The overall probability of detecting rocks with diameters ≥ 5 pixels was 85% with an average of 3 false alarms per image. Perfect performance (100% detection with no false alarms) was achieved for rocks ≥ 25 pixels in diameter. These results are useful to choose the camera field of view and operating altitude to achieve a desired level of reliability. For example, if hazardous rocks have diameters >= 1 m, operation is at at 200m altitude, and a performance equivalent to the 25 pixel diameter case in Figure 9 is desired, the camera angular resolution must be 0.2 millirads/pixel.

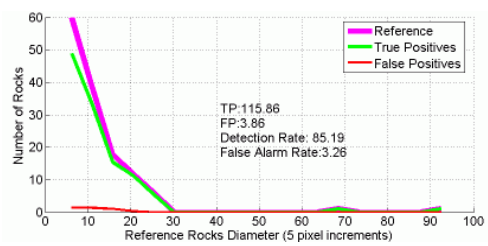

Figure 10. Shadow-based rock detection. Average detection for seven different sun angles. Shadow regions are >= 5 pixels.

Since true rock height was not available with this dataset a number of experiments were conducted using the wall dataset. Figure 11 shows a result for a simulated wall image at 400m distance. The GSD for this image is 11.2cm and the RMSE of the difference between the measured height (magenta bars) and actual rock heights (cyan bars) is 1.8cm, i.e. 5.4% of the average true height (33cm) of the rocks.

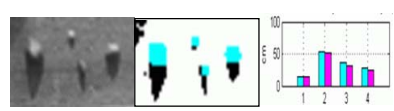

Figure 11. Shadow-based rock detection from wall dataset simulated to 400m altitude. The chart compares true (cyan) to estimated (magenta) rock height.

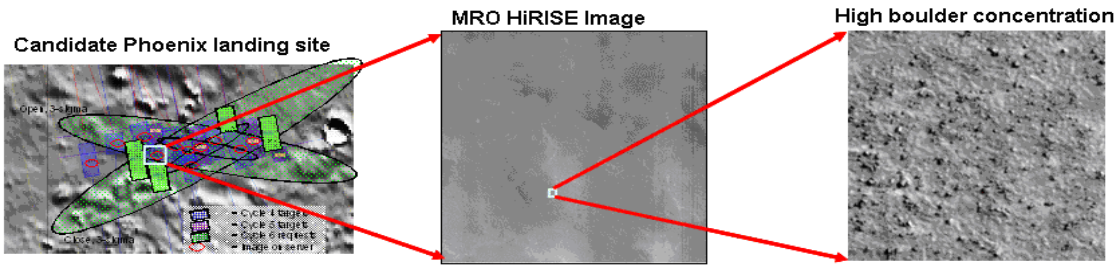

Figure 12. Candidate landing ellipses and HiRISE image coverage for one area in the Phoenix mission. Rocks >1 meter are clearly visible. Images are 20,048 pixels across (6km).

The Mars Reconnaissance Orbiter (MRO) entered Mars orbit in the Fall of 2006. Among its instruments it carries the High Resolution Image Science Experiment (HiRISE) instrument. From an altitude of 300 km and with an FOV of 1.14° x 0.18° it is capable of acquiring image swaths 20,264 pixels across at 0.3 m/pixel (Figure 12). The swath length is typically twice the swath length, thus covering an area 6.2 km x 12.4 km. The instrument was targeted from December 2006 to March of 2007 to acquire high resolution images overlapping three potential landing sites for the Phoenix Mission, scheduled for landing in May of 2008. The 36 GByte HiRISE dataset (46 images) covers an area of approximately 1,500 km^2. At this resolution and given the favorable sun elevation angles (~60° incidence,) the shadow-based rock detection algorithm was applied to map large rocks accurately, on the order of 1m or larger.

The rock mapping algorithm, derived from the real-time HD algorithm described above affords the additional computational cost needed for a more refined analysis of the shadows detected at the available GSD and the processing of the very large images. These include analyzing the detected shadow regions in more detail to attempt to separate merged shadows from adjacent rocks, and analysis of the illumination boundary between the rock and its self shadow. Certain terrain features in the scale of the lander cast shadows comparable to those of rocks. Many of these features are elongated and can be discerned from the aspect ratio of their shadows but some are fragmented features and have sizes consistent with large rocks. The analysis of the illumination gradient along the illumination terminators, however, has been highly successful in discriminating these fragments from large rocks. The mapping algorithm generates a rock description record (position and size of individual shadows and rock models) for an entire HiRISE image in a few minutes. Overall, over 10 million rocks were detected and mapped. Figure 12 shows one of three 150km x 75km areas designated for analysis.

With such large areas under consideration, we expect variations in the terrain. Figure 13 illustrates five representative terrain types in the dataset. Four of them represent areas away from craters whereas the areas near, even filled, craters typically have large concentrations of rocks, many of them large boulders. Figure 14 illustrates a result of rock detection from a small portion of a HiRISE image. The shadows detected (>= 5 pixels) are illustrated on the right bottom by their approximated ellipses.

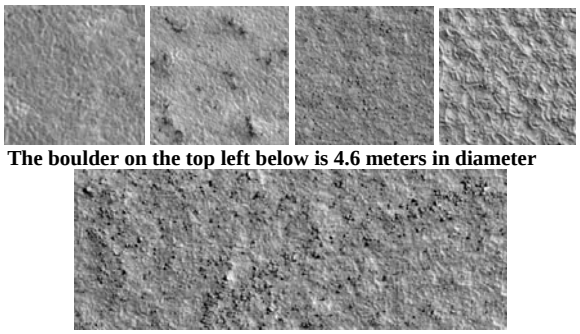

Figure 13. terrain types. Top row: polygonal (5-10cm relief at edges) with very few rocks, Boulder clusters interspersed with boulder-free polygonal terrain, Low to medium-density rocks uniformly distributed across surface and Rippled terrain with very few rocks or rock-free. Bottom: Rocks along border of filled-in craters.

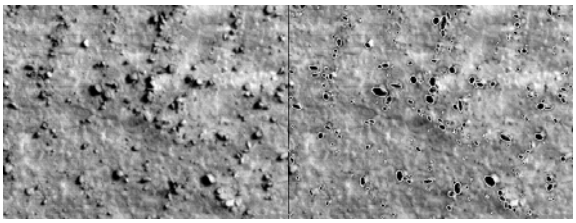

Figure 14. Detail of rock field and shadows detected and approximated by ellipses. The smallest rock diameter is ~70 cm.

Figure 15 illustrates results for an entire HiRISE image covering ~6km x 18km. Density and thematic maps are derived from the full rock population of 260 thousand rocks in a straight forward manner at any level of granularity. In this example the map cells are 100m x 100m. The color scale of the density map (center) represent number of rocks having diameters >= 1m. The color scale of the thematic map (left) denotes ranges of rock density related to rock abundance.

For validation we compared automatic detection

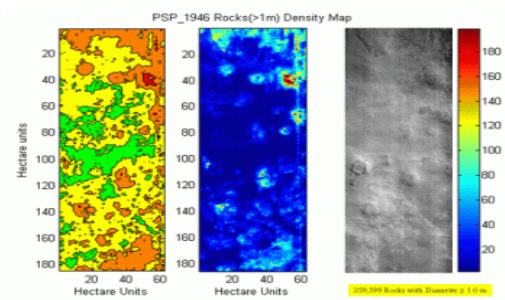

Figure 15. The HiRISE image (right) covers an area 6km across x 18km. The color-coded density map (center) represents number of rocks >= 1m in hectare cells. The thematic map (left) encodes density related to rock abundance and cumulative fractional area (CFA, [9]) covered by rocks.

with manual counts from HiRISE sub-images provided by Prof. R. Arvidson of Washington University, and compared to counts from surface imagery provided by M. Golombek of JPL. Surface counts are from previous efforts to derive rock distribution models at the landing sites of previous Mars missions, e.g. Viking Landers (VL1 and VL2) [9]. For automatic counts we used portions of HiRISE images of the landing sites. Figure 16 illustrates one such comparison for the VL2 landing site. The black and red plots are for surface and manual counts respectively. The three remaining and overlapping plots are for automatic counts.

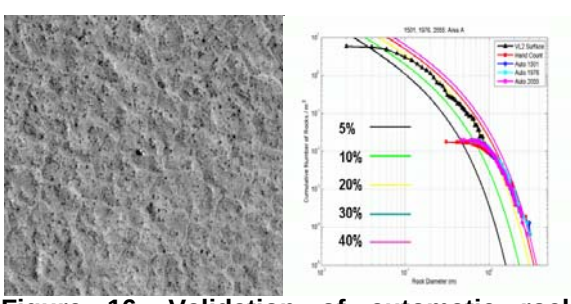

Figure 16. Validation of automatic rock detection. VL2 is at center of image. The plots represent rock distributions. The automatic counts follow very well the exponential distribution model in [9].

5. Safe Landing Probability Model

A great deal of work has been dedicated to Martian rock distributions and selecting safe landing sites on Mars over the last few years [9]. The distributions model (also called rock abundance model), is given in terms of the cumulative fractional area covered by rocks as a function of rock diameter. Martian rock abundance varies from 0% to 40%. The MSL mission

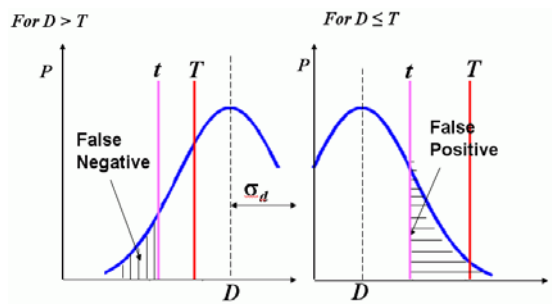

Figure 17. Uncertainty in the diameter (or height) of a detected rock is modeled by a Gaussian distribution, *T* represents the lander hazard threshold and *t* represents the HAD algorithm hazard threshold.

is targeting to land a rover to the terrain less than 10% rock abundance with landing failure probability due to rock impalement less than 0.25%.

The model we have developed is suitable for both stereo and shadow-based rock detection. Mathematical details are given in [4]. Errors are influenced by different factors and are assumed to follow Gaussian distributions. For example, the shadow-based rock detection error varies from 10%, mostly dependent on sun aureole effects, to 50% for the worst case rock shape, i.e. a hemispherical rock. The range is valid for Sun incidence angles between 30° and 70°.

Referring to Figure 17, the probability of false negatives and the probability of false positives are given by integrating the tails of the Gaussian distribution. The probability of successful HD landing is given by the probability that a safe site exists times the probability of finding it (details in [4].)

The analytical model of probability of a successful landing provides a tool not only to estimate such probabilities but also to compare blind landing to landing with hazard detection vision capabilities. Figure 18 shows plots of such comparison instantiated for MSL mission parameters, i.e., a rock tolerance, or mechanical threshold *T*, of 60cm, and a $4m^2$ lander undercarriage. The stereo HD plot (green) is for a sensing altitude of 70m. Note that this prediction is consistent with the wall results at 70m observed in the error propagation model described in Section 4 (Figure

9) for the wall dataset. The safe landing probability predictions applied to shadow-based detection are also illustrated in Figure 19. The blue plot corresponds to the 5.4% height errors from the wall dataset at a simulated 400m altitude (see also Figure 11.) The red plot corresponds to a worst-case shape idealized hemispherical rocks illuminated by a 50° Sun incidence angle, and assumes that 30% of rocks are pyramidal, i.e., not detected because they do not cast shadows. Note however the doubling of rock abundance for a given level of safety. The MSL probability goal is at 0.9975%.

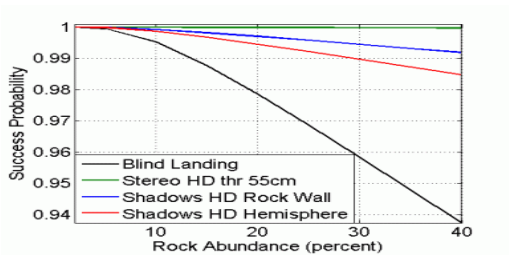

Figure 18. Landing with HD capability compared to blind landing (black plot) instantiated for MSL parameters. The success probability is the product of the probability of no detections and the probability of no missed detections. The green plot predicts stereo-based probability with sensing from 70m altitude. The blue plot is for shadow-based detection from the wall simulated 400m altitude. The red plot is for shadow based idealized hemispherical rocks at 50° incidence illumination.

6. Conclusion

We used a Mars landing scenario as an extreme case of a fast, near-vertical descent to motivate sensor selection for landing hazard detection. This and considerations of minimizing mass, power, and volume while maximizing relevance to other missions led us to conclude that stereo vision and shadow analysis with descent cameras appear to be the smallest sensor suite with the widest applicability, given the state of development of sensor alternatives today. We then outlined algorithms we have developed to date to detect slope hazards with stereo vision and rock hazards with stereo vision and shadow analysis. We derived analytical performance models for these based on Gaussian noise models, compared the prediction of those models to experimental data, and found reasonably good agreement. This implies that the models are useful for predicting performance of these functions in operational scenarios. Therefore, we then embedded the hazard detection performance models in a model for the probability of landing safely, given parameterized models of lander rock tolerance, lander area, and parameterized rock size/frequency distributions fit to Mars and terrestrial data. When this model is instantiated for parameters of the MSL mission, it predicts that even very conservative assumptions about the performance of the vision system will reduce the probability of a failed landing by at least a factor of four compared to a blind landing for any rock abundance. Conversely, for the level of safety desired by MSL, it predicts that the vision system would allow access to roughly triple the fraction of the planet as a blind landing. This would represent a major improvement in access to sites of scientific value for a small increase in sensor payload. Analogous benefits should accrue to missions to other bodies in the solar system.

9. Acknowledgments

The research described was carried out at the Jet Propulsion Laboratory, California Institute of Technology, sponsored by the Mars Technology Program under NASA Mars Exploration Program Advanced Technologies NRA (*OSS-03-01)* and NASA New Millennium Program (NMP) ST9.

10. References

[1] Andrew E. Johnson, Allan Klumpp, James Collier and Aron Wolf, **"**Lidar-based Hazard Avoidance for Safe Landing on Mars**,"** *AIAA Journal of Guidance, Control and Dynamics* 25 (5), October 2002.

[2] A. Huertas, Y. Cheng, & R. Madison, "Passive Imaging Based Multi-cue Hazard Detection for Spacecraft Safe Landing," *Proc. IEEE Aerospace Conf.*, Big Sky, MO. Mar. 2006.

[3] L. Matthies, A. Huertas, Y. Cheng and A. Johnson, "Landing Hazard Detection with Stereo Vision and Shadow Analysis," *Proc. Infotech@Aerospace2007 Conference*, Rohner Park, CA, May 2007.

[4] A. Huertas, Y. Cheng and L.Matthies, "Real-time Hazard Detection for Landers," *Proc. NASA Science Technology Conf.*, Adelphi, MD, May 2007.

[5] J. Vevrka et. al. "Imaging of Small-Scale Features on 433 Eros from NEAR: Evidence for a Complex Regolith," *Science*, Vol. 292. no. 5516, Apr. 2001, pp. 484 – 488.

[6] P. Christensen, et al "Morphology and Composition of the Surface of Mars:Mars Odyssey THEMIS Result", *Science* 300, 2056 (2003).

[7] H. Hirschmueller, P. Innocent, and J. Garibaldi, "Real-time correlation-based stereo vision with reduced border errors," *Int'l Journal of Computer Vision*, vol. 47, no. 1-3, pp. 229.246, April-June 2002.

[8] Harold W. Sorenson "Parameter Estimation", Marcel Dekker, Inc.1980.

[9] M. Golombek, et. al., "Rock Size-Frequency Distributions on Mars and Implications on Mars Exploration Rover Landing Safety and Operations," *Journal of Geophysical Research*, Vol. 108, No. E12, 2003.